Journal of Microscopy, Vol. 182, Pt 1, April 1996, pp. 50–60.
Received 13 June 1995; accepted 17 November 1995

Dispersion, aberration and deconvolution in multi-wavelength fluorescence images

B. A. SCALETTAR,*† J. R. SWEDLOW,*[1] J. W. SEDAT* & D. A. AGARD*
**Howard Hughes Medical Institute, and Graduate Group in Biophysics, and the Department of Biochemistry and Biophysics, University of California, San Francisco, San Francisco, CA 94143-0448, U.S.A.*
†Department of Physics, Lewis and Clark College, Portland, OR 97219, U.S.A.

Key words. Point-spread function, dispersion, spherical aberration, iterative deconvolution, fluorescence microscopy.

Summary

The wavelength dependence of the incoherent point spread function in a wide-field microscope was investigated experimentally. Dispersion in the sample and optics can lead to significant changes in the point spread function as wavelength is varied over the range commonly used in fluorescence microscopy. For a given sample, optical conditions can generally be optimized to produce a point spread function largely free of spherical aberration at a given wavelength. Unfortunately, deviations in wavelength from this value will result in spherically aberrated point spread functions. Therefore, when multiple fluorophores are used to localize different components in the same sample, the image of the distribution of at least one of the fluorophores will be spherically aberrated. This aberration causes a loss of intensity and resolution, thereby complicating the localization and analysis of multiple components in a multi-wavelength image. We show that optimal resolution can be restored to a spherically aberrated image by constrained, iterative deconvolution, as long as the spherical aberration in the point spread function used for deconvolution matches the aberration in the image reasonably well. The success of this method is essentially independent of the initial degree of spherical aberration in the image. Deconvolution of many biological images can be achieved by collecting a small library of spherically aberrated and unaberrated point spread functions, and then choosing a point spread function appropriate for deconvolving each image. The co-localization and relative intensities of multiple components can then be accurately studied in a multi-wavelength image.

[1]Present address: Department of Cellular and Molecular Pharmacology, University of California, San Francisco, San Francisco, CA 94143-0450, U.S.A.
*Correspondence: David A. Agard.

Introduction

In the last decade, the optical microscope has evolved into a powerful three-dimensional imaging tool (Agard, 1984; Fay *et al.,* 1989; Denk *et al.,* 1990; Hiraoka *et al.,* 1991; Taylor *et al.,* 1992). This advance has been spurred largely by developments in microscope technology and in computational image processing techniques. Specifically, the development of optical microscopes whose focal position can be precisely and automatically incremented has made it possible to generate three-dimensional images by stepping through focus and collecting a series of two-dimensional 'optical sections' of a three-dimensional object (Agard, 1984; Castleman, 1979; Fay *et al.,* 1989; Liu & Holmes, 1993). Moreover, the development of the confocal microscope (Pawley, 1995) and computational image-processing techniques based on deconvolution (Agard, 1984; Agard *et al.,* 1989; Fay *et al.,* 1989; Liu & Holmes, 1993) have largely eliminated problems associated with intensity blurring in some forms of optical microscopy, most notably fluorescence microscopy, and have markedly enhanced the resolution obtained with the optical microscope.

An important problem in three-dimensional imaging is the blurring of object intensity, primarily by the objective lens of the microscope. The blurring is described by the image of a theoretical point source of light and is known as the point spread function (PSF) of the microscope (Castleman, 1979; Agard, 1984). If a microscope were an ideal imaging system, the PSF would be a point. Unfortunately, limitations on the collection of spatial frequencies imposed by the objective aperture and path length errors introduced by out-of-focus components combine to produce blurring in the PSF. In addition, uncorrected aberration in the optical components can further degrade the PSF (Born & Wolf, 1980; Inoue, 1986; Hiraoka *et al.,* 1990a; Gibson & Lanni, 1991). Thus, the empirical PSF is not a point; instead, for a

high numerical aperture (NA) objective lens it extends over *c.* 0·4 μm in the image plane and over *c.* 5 μm along the optical axis (Inoue, 1986; Hiraoka *et al.,* 1990a). This blurring of intensity from a point object implies that all optical images will be similarly blurred.

For an arbitrary three-dimensional object, an optical microscope yields an image intensity distribution, $i(x,y,z)$, that to a good approximation is given by the convolution of the object intensity distribution, $o(x,y,z)$, with the PSF (Castleman, 1979; Agard, 1984). Thus

$$i(x,y,z) = o(x,y,z) \otimes \mathrm{PSF}(x,y,z) \qquad (1)$$

where the $\otimes$ symbol denotes the convolution operation, x and y are orthogonal axes in the image plane, and z is the optical axis. Equation (1) can be used to obtain an estimate of the true (unblurred) distribution of intensity in the object from a measured image intensity distribution and PSF; this is the goal of three-dimensional image reconstruction algorithms (see, for example, Agard *et al.,* 1989). One commonly used reconstruction algorithm, constrained iterative deconvolution, generates an estimate of the object based on a comparison of the image with the convolution of the estimate and the PSF (Agard, 1984). Alternative reconstruction schemes include those based on maximum likelihood estimation (Conchello & Hansen, 1990; Liu & Holmes, 1993; Willis *et al.,* 1993), combinations of multiple views (Shaw, 1990), least-squares techniques (Carrington, 1990), and projection onto convex sets (Koshy *et al.,* 1990).

Since PSFs describe the imaging characteristics of optical microscopes, they have been the subject of detailed theoretical and experimental study. Theoretical analyses show that the PSF of an ideal diffraction-limited optical system will possess both radial and axial symmetry (Born & Wolf, 1980), i.e. $\mathrm{PSF}(x,y,z) = \mathrm{PSF}(r,z) = \mathrm{PSF}(r-z)$, where $r = (x^2 + y^2)^{1/2}$. In addition, theoretical analyses show that aberrations in the optical system, such as spherical aberration, astigmatism, coma and field curvature, affect the PSF (Born & Wolf, 1980; Castleman, 1979). In particular, spherical aberration is predicted to lead to a loss of axial symmetry (Born & Wolf, 1980; Gibson & Lanni, 1991).

Recent experimental measurements of PSFs for fluorescence microscopy have revealed that empirical PSFs frequently exhibit strong radial and axial asymmetry, and thus differ significantly from the theoretical diffraction-limited PSF (Hiraoka *et al.,* 1990a; Gibson & Lanni, 1991). Moreover, axial asymmetry has been shown to be due to spherical aberration that arises from an improper optical path length (Hiraoka *et al.,* 1990a; Gibson & Lanni, 1991). For example, when the optical path length is altered experimentally by changing the refractive index of the objective immersion oil by $\geq 0{\cdot}002$ units, the intensity distribution along the optical axis is significantly perturbed. For a given sample, objective lens and wavelength of light, one particular 'ideal' refractive index of the immersion oil produces a PSF with the highest degree of axial symmetry and the most rapid intensity decay along the axial direction (Hiraoka *et al.,* 1990a). Non-ideal refractive indices produce a spherically aberrated PSF with less axial symmetry and a less rapid intensity decay along the axial direction (Inoue, 1986; Hiraoka *et al.,* 1990a; Gibson & Lanni, 1991). In wide-field microscopy, a less rapid intensity decay increases blurring and leads to a loss in axial resolution. In confocal microscopy, a less rapid intensity decay leads to loss of resolution and, perhaps more dramatically, to a loss of signal (Hell *et al.,* 1993).

In this report, we extend previous experimental studies by showing that PSFs of high-NA oil-immersion objectives can have significant wavelength dependence. We illustrate this effect in images of fluorescent beads of different colours and in multi-wavelength images obtained from biological samples that have been labelled with several different fluorophores. This wavelength dependence arises in lenses that are nominally corrected for chromatic and spherical aberrations. We attribute the wavelength dependence of the PSF to the difficulty of obtaining perfect chromatic correction of the lenses, given that the refractive indices of all elements of the optical path, including the sample, are wavelength dependent. For example, the refractive index of a typical immersion oil changes from 1·5239 to 1·5115 as wavelength varies over a range commonly used in fluorescence microscopy (486–656 nm; Cargille, 1994). We further show that deconvolution with appropriate PSFs — even spherically aberrated ones — can be used to correct the different wavelength components of a multi-wavelength image. Methods of dealing with the complexities encountered in deconvolving multi-wavelength images, and spherically aberrated images in general, are developed and discussed.

Materials and methods

Sample preparation

Samples consisting of 0·12-μm-diameter dark red beads (excitation maximum = 650 nm; emission maximum = 690 nm) or yellow/green beads (excitation maximum = 490 nm; emission maximum = 515 nm) (Molecular Probes, Eugene, OR) were prepared by diluting a stock suspension (2% solids) of beads one-million-fold with ethanol and then depositing 10 μL of the solution onto a 22-mm × 22-mm 1½ Gold Seal coverslip (Becton Dickinson, Lincoln, NJ). The ethanol was evaporated by warming the coverslip to 40 °C on a slide warmer, causing the beads to adhere directly to the coverslip. Seven microlitres of a solution consisting of 2% N-propyl gallate in glycerol (for green beads, 50 mM Tris base, final pH 8·0) were then deposited over the beads. The coverslip was gently placed on a slide and sealed to the slide with clear nail enamel (Wet and Wild, Pavion Ltd,

Nyack, NY). A minimum of 6 h was allowed to elapse before data collection was initiated to ensure that the enamel was dry and that the sample was as immobile as possible.

Instrumentation and data collection

Our wide-field three-dimensional fluorescence imaging system (Hiraoka *et al.*, 1991) is built around an Olympus inverted microscope (Olympus, Lake Success, NY). The microscope stage is under the control of a Nanomover microstepper motor (Melles Griot, Irvine, CA), which permits the z position of the stage to be adjusted automatically in increments as small as 0·1 μm. For the experiments described here, the wavelengths of the excitation and emission light were controlled using appropriate excitation/emission filter pairs and a triple multichroic mirror designed for use with the fluorophores Texas Red, fluorescein isothiocyanate (FITC) and 4′,6-diamidino-2-phenylindole (DAPI) (Chroma Technology, Brattleboro, VT). The filters are anti-reflective coated and blocked in the ultraviolet and infrared; their band passes are: FITC (EX/EM 485 ± 22 nm/535 ± 45 nm) and Texas Red (EX/EM 560 ± 55 nm/635 ± 60 nm). Since the z focus and filters are under computer control, it is possible to collect three-dimensional multi-wavelength images rapidly.

Three-dimensional images of beads and biological samples were collected on a cooled, 12-bit charge-coupled device (CCD) camera (Photometrics, Tucson, AZ), using either a 60×/1·4-NA oil-immersion objective (Olympus) or a 100×/1·4-NA oil-immersion objective (Nikon, Melville, NY). Immersion oils of specified refractive index at 589·3 nm and 25 °C (denoted n_D^{25}) were generated by appropriately mixing Cargille Laser Liquids from series 5610 (Cargille Laboratories, Cedar Grove, NJ). All data were collected at a temperature of $23 \pm 0{\cdot}5$ °C, so the n_D^{25} values cited throughout this paper are for relative comparison only. Three-dimensional images of beads were generated by collecting four images of a bead at each of 80 different focal positions differing in increments of 0·1 μm; the four images corresponding to a given focal position were later averaged to enhance accuracy. Averaging is used instead of increasing the exposure time because the signal from the beads when in focus nearly saturates the CCD after a brief exposure. Three-dimensional images of biological samples were generated by collecting 64 images at focal positions differing in increments of 0·2 μm. Slight variations in the gain and offset of the pixels on the CCD, and temporal variations in lamp intensity, were corrected for as described previously (Hiraoka *et al.*, 1991; Chen *et al.*, 1995).

Deconvolution algorithm

Images of beads and biological samples were deconvolved using a constrained iterative deconvolution algorithm (Agard *et al.*, 1989). In this algorithm, convolution operations are carried out using the Fourier transform of Eq. (1), which reads (Castleman, 1979)

$$I(k_x, k_y, k_z) = O(k_x, K_y, K_z) \cdot \mathrm{OTF}(k_x, k_y, k_z) \qquad (2)$$

Here, $I(k_x, k_y, k_z)$, $O(k_x, k_y, k_z)$ and the optical transfer function $\mathrm{OTF}(k_x, k_y, k_z)$ are the Fourier transforms of $i(x, y, z)$, $o(x, y, z)$ and $\mathrm{PSF}(x, y, z)$, respectively, k_x, k_y and k_z are the Fourier variables corresponding to x, y and z, and the symbol $\cdot$ represents multiplication. Equation (2), rather than Eq. (1), is used because it reduces the convolution operation to a simple multiplication in Fourier space. While it is possible to use a theoretical OTF in the deconvolution algorithm (Frieden, 1969; Agard, 1984), best results have been obtained using an OTF calculated from a measured PSF (Hiraoka *et al.*, 1990a).

One recent modification to our deconvolution algorithm ensures proper deconvolution with OTFs generated from spherically aberrated (axially asymmetric) PSFs. Previously, the algorithm used *real*, radially averaged OTFs having the symmetry property $\mathrm{OTF}(k_r, -k_z) = \mathrm{OTF}(k_r, k_z)$ ($k_r = [k_x^2 + k_y^2]^{1/2}$). These were generated by direct three-dimensional Fourier transformation of unaberrated, axially symmetric PSFs, followed by radial averaging of the amplitude of the Fourier transform over the variables k_x and k_y (Hiraoka *et al.*, 1990a). This procedure is valid only if spherical aberration in the PSF is negligible. To deal correctly with spherically aberrated PSFs, OTFs are now computed by radially averaging the full complex Fourier components of a spherically aberrated PSF; this procedure yields *complex* OTFs having the symmetry property $\mathrm{OTF}(k_r, -k_z) = \mathrm{OTF}^*(k_r, k_z)$, where the asterisk denotes complex conjugation. The introduction of a complex OTF into the deconvolution algorithm ensures a correct treatment of axial asymmetry in the PSF, although radial averaging ignores radial asymmetry. We have continued to neglect radial asymmetry because it is generally less prominent than axial asymmetry. In addition, introduction of an angle-dependent OTF could introduce noise that is currently suppressed by radial averaging.

An additional issue that arises when the OTF is complex is that OTF phases are influenced by the position of the associated PSF in image space. The correct OTF phases will be obtained only if the centre of mass of the PSF is at the origin of the image-space coordinate system. If the centre of mass is not at the origin $(0, 0, 0)$ of image space, but instead has coordinates (X, Y, Z), the phase of $\mathrm{OTF}(k_x, k_y, k_z)$ will be incorrect; however, the phase can be corrected by multiplying by the factor $\exp[-2\pi i(k_x X + k_y Y + k_z Z)]$.

Image analysis

Four quantities were used to characterize the quality of a

deconvolved image: (i) R factor, (ii) contrast, (iii) power (frequency) spectrum and (iv) axial resolution. The R factor is defined as

$$R = \frac{\sum_{i,j,k} |Image(i,j,k) - Guess(i,j,k) \otimes PSF|}{\sum_{i,j,k} |Image(i,j,k)|} \qquad (3)$$

where $Guess(i,j,k)$ is the distribution of intensity in the deconvolved image, and the sum is over all points in the image. (The terminology guess is used because deconvolution yields a 'guess' at the true distribution of intensity in the object (Agard *et al.,* 1989).) Contrast, C, is defined as

$$C = \sum_i \sum_j [Guess(i,j,k) - \langle Guess(i,j,k)\rangle]^2$$

where $\langle Guess(i,j,k)\rangle$ is the average intensity of the eight adjacent neighbours of point (i, j) in optical section k. The radially averaged power spectrum, $P(k_r, k_z)$, of an image is defined as the radial average of the absolute square of the three-dimensional Fourier transform of the image (Castleman, 1979). Axial resolution in a point image is defined as the half-width of a plot of the integrated intensity in each section vs. focal position (Hiraoka *et al.,* 1990a).

Results

Lens-dependence of the PSF

Because PSFs play an essential role in accurate reconstruction of the object intensity distribution, considerable effort has been directed at measuring and characterizing their properties (Hiraoka *et al.,* 1990a; Gibson & Lanni, 1991; Shaw & Rawlins, 1991; Hell *et al.,* 1993). Here we have investigated the dependence of PSF spherical aberration on choice of objective lens and wavelength. Strictly speaking, we measure the PSF of the entire microscope, but the characteristics of the PSF are essentially determined by the optical properties of the sample and the objective lens.

We have found significant differences between PSFs obtained from different high-NA lenses. For example, the optimal (least spherically aberrated) PSF collected at 635 nm

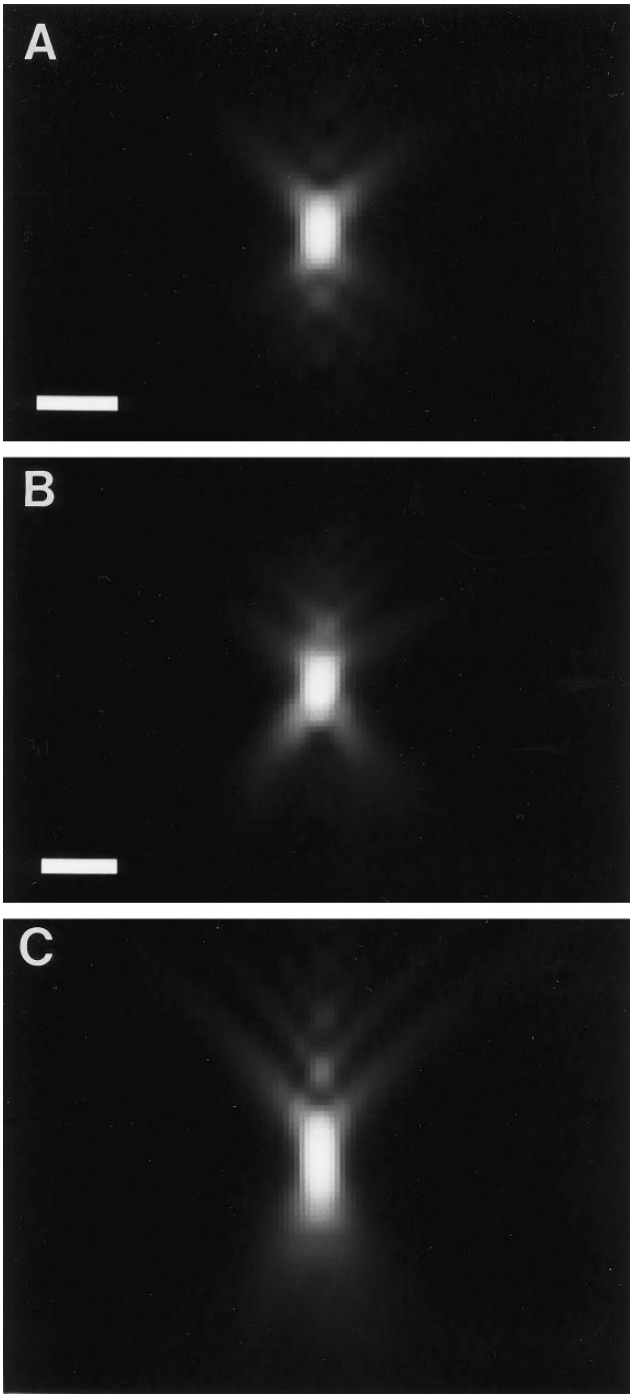

Fig. 1. Lens Dependence of PSFs. Orthogonal views of PSFs from a Nikon 100×/1·4-NA objective (A) and an Olympus 60×/1·4-NA objective (B,C) collected using 635-nm light. (A) PSF collected using an immersion oil with $n_D^{25} = 1{\cdot}5150$. (B) PSF collected using an immersion oil with $n_D^{25} = 1{\cdot}5140$. (C) PSF collected using an immersion oil with n_D^{25} \Psi $= 1{\cdot}5230$. This oil yields an optical path length that is too long and an image that is spherically aberrated. Scale bars = 1 μm. (D) Integrated intensity profiles for the PSFs shown in (A; △), (B; ●), and (C; ○). The optical axis is parallel to the vertical axis of the image.

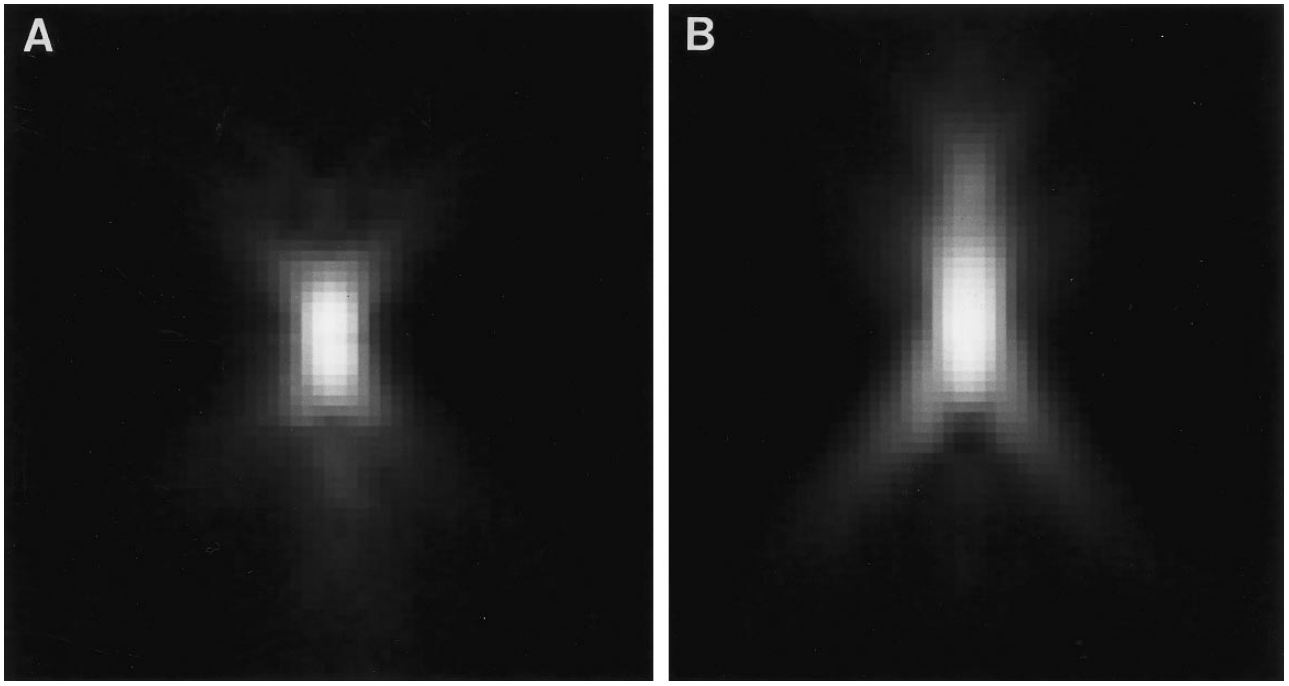

Fig. 2. Wavelength dependence of PSFs. Orthogonal views of PSFs from an Olympus 60×/1·4-NA objective collected using an immersion oil n_D^{25} = 1·5128 and (A) 535-nm light or (B) 635-nm light. The PSF in (A) shows approximate axial symmetry; the PSF in (B) shows strong axial asymmetry, or spherical aberration.

with a 100×/1·4-NA Nikon objective has considerably greater radial and axial symmetry than the optimal PSF collected with a 60×/1·4-NA Olympus objective (Fig. 1A,B). This implies that the 100× objective has less intrinsic spherical aberration than the 60× objective, yielding under optimal imaging conditions a PSF more like that produced by an ideal, diffraction-limited lens. The improved axial resolution of the 100× Nikon objective is shown graphically by a plot of the integrated intensity of the PSFs along the optical axis (Fig. 1D).

For a given high-NA lens and wavelength, significantly different PSFs can also be generated by altering optical path length. This is most conveniently accomplished by changing the refractive index of the objective immersion oil (Hiraoka *et al.*, 1990a). Results obtained with the 60× objective at 635 nm are shown in Fig. 1(B,C). Here an oil with an n_D^{25} of 1·5140 yields an optimal optical path length, characterized by a relatively symmetric, unaberrated PSF. Oils with higher or lower n_D^{25} yield positive or negative optical path length errors, as indicated by axially asymmetric, spherically aberrated PSFs (Fig. 1C). Specifically, a positive optical path length error yields a PSF with excess intensity in sections collected when the objective lens is furthest from the coverslip, whereas a negative optical path length error yields a PSF with excess intensity in sections collected when the objective lens is closest to the coverslip (Hiraoka *et al.*, 1990a).

Wavelength dependence of the PSF

We have also found that for a given objective and immersion oil, the degree of spherical aberration in the PSF varies significantly as wavelength is varied over a spectral range common in fluorescence microscopy (Fig. 2). For example, for the 60× Olympus objective, an oil with an n_D^{25} of 1·5128 yields an unaberrated PSF when measured at 535 nm, and a very spherically aberrated PSF when measured at 635 nm. For the same objective, a fairly unaberrated PSF can be obtained at 635 nm if the n_D^{25} of the oil is 1·5140 (Fig. 1B). Similar wavelength-dependent effects were observed with the Nikon lens (data not shown). In comparing PSFs from these two wavelengths, we noticed residual uncorrectable spherical aberration in the Olympus 60× lens at 635 nm, but not at 535 nm (compare Figs 1B and 2A). This behaviour was not observed using the Nikon 100× lens.

The dependence of PSFs on wavelength can be at least qualitatively attributed to changes in optical path length induced by changes in refractive indices with wavelength. Refractive indices typically decrease with increasing wavelength; thus, if the optical path length is correct for a given sample, optical configuration and wavelength, an increase in wavelength would be expected to produce an optical path length that is too short and a decrease in wavelength would be expected to produce an optical path length that is too long. This would imply that the optimal PSF at 535 nm

would be obtained with an oil of lower n_D^{25} than the optimal PSF at 635 nm. This is exactly the trend that we have observed experimentally (Fig. 2).

These observations have important consequences for multi-wavelength fluorescence images of any sample. Different wavelength components of a multi-wavelength image will have different PSFs. Moreover, using a single choice of immersion oil, the PSF can only be optimized at one wavelength—data collected at other wavelengths will be spherically aberrated. Since axial resolution in an aberrated image is significantly degraded (Figs 1 and 2), it is important to determine how well deconvolution can enhance resolution and reverse spherical aberration in spherically aberrated images.

Effects of spherical aberration on deconvolution

The effects of spherical aberration on image restoration were tested by deconvolving spherically aberrated PSFs with various OTFs and analysing how well the deconvolved images approximated a point. The point-like character of an image was determined by calculating power spectra and by plotting the integrated intensity in each optical section as a function of focus. A narrow, symmetric intensity decay, together with a broad power spectrum, indicated a good reconstruction of a point.

We have collected a small library of PSFs for each of our two high-magnification (60× and 100×) objectives, using 635-nm and 535-nm beads and oils with n_D^{25} between

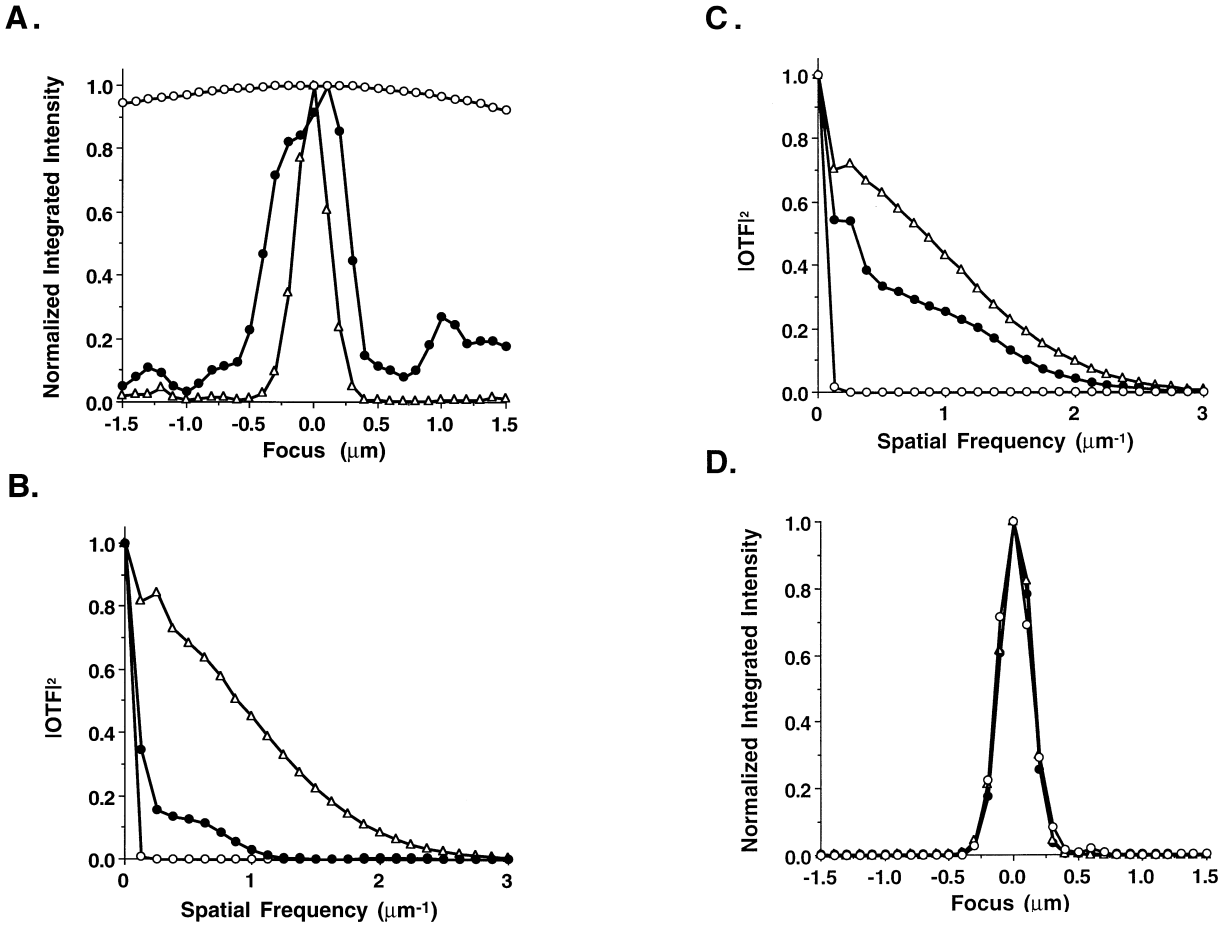

Fig. 3. Resolution enhancement obtained from deconvolution of spherically aberrated bead images. A library of PSFs/OTFs was collected and used to compare the resolution enhancement obtained deconvolving spherically aberrated and unaberrated images. (A) Integrated intensity decays for a spherically aberrated 60× PSF ($n_D^{25} = 1{\cdot}5230$). (B) Radially averaged power spectrum, $|\mathrm{OTF}(k_r = 0, k_z)|^2$, for a spherically aberrated 60× PSF ($n_D^{25} = 1{\cdot}5230$). (C) Radially averaged power spectrum for an unaberrated 60× PSF ($n_D^{25} = 1{\cdot}5140$). (○) Before deconvolution; (●) after deconvolution of the PSF with the real OTF; (△) after deconvolution of the PSF with the complex OTF derived from it. Deconvolution with a complex OTF produces an image with a power spectrum that extends out to 3 μm^{-1} along the k_z axis. (D) Integrated intensity decays obtained after deconvolving a broad spectrum of aberrated and unaberrated PSFs with their associated complex OTFs. The half-width of the decay after deconvolution is essentially independent of half-width before deconvolution, increasing slightly as the PSF becomes heavily aberrated. (○) $n_D^{25} = 1{\cdot}5104$; (●) $n_D^{25} = 1{\cdot}5140$; (△) $n_D^{25} = 1{\cdot}5230$.

1·5000 and 1·5572. For each objective and wavelength, one PSF was essentially free of spherical aberration; the others were aberrated to various degrees. As a first test of deconvolution of spherically aberrated images, each of these PSFs was deconvolved with its associated complex OTF (i.e. its radially averaged Fourier transform) and with a real OTF obtained from the corresponding lens under optimal imaging conditions. The images obtained from the complex and real deconvolutions are compared in Fig. 3(A).

Comparison of the real and complex deconvolutions of an aberrated PSF (n_D^{25} = 1·5230) shows that the real deconvolution yielded an image with a two-fold wider half-width and a power spectrum with a two- to three-fold smaller cut-off frequency and a reduced overall frequency content (Fig. 3A,B). By contrast, comparison of the real and complex deconvolutions of a relatively unaberrated PSF (n_D^{25} = 1·5140) shows little difference in half-widths (data not shown) and cut-off frequencies (Fig. 3C); however, the overall frequency content obtained from the real deconvolution was again somewhat reduced. These results show that spherically aberrated images are poorly deconvolved by a real OTF obtained from an unaberrated PSF.

The above results also suggest that spherically aberrated images can be effectively deconvolved if an appropriate complex OTF is used. In Fig. 3(D) we demonstrate this explicitly. When unaberrated and spherically aberrated PSFs were deconvolved with their associated complex OTFs, all the resulting integrated intensity plots had the same axial half-width, 0·25 μm, independent of the initial degree of spherical aberration in the PSF. This result held over a broad range of optical path lengths; thus, the resolution of spherically aberrated images can be dramatically enhanced through deconvolution if an appropriate complex OTF is used.

For PSF images, the optimal OTF is easily calculated from the Fourier transform of the image itself; unfortunately, for a typical biological image an appropriate OTF is not so easily identified. Methods have been developed that allow estimation of the PSF/OTF from a biological image (Liu & Holmes, 1993); nevertheless, there frequently will be some uncertainty about the choice of OTF, and for this reason we have analysed the effect of OTF mismatch on deconvolution efficiency.

Effect of PSF/OTF mismatch on deconvolution

To test the effect of OTF mismatch on deconvolution performance, PSFs were deconvolved not only with their associated complex OTFs and the real OTF, as described above, but also with complex OTFs derived from other, mismatched, PSFs. Thus, spherically aberrated PSFs resulting from short and long optical path lengths were deconvolved with a number of complex OTFs derived from PSFs manifesting the same, or the opposite, type of spherical aberration (Fig. 4).

When spherically aberrated PSFs were deconvolved with

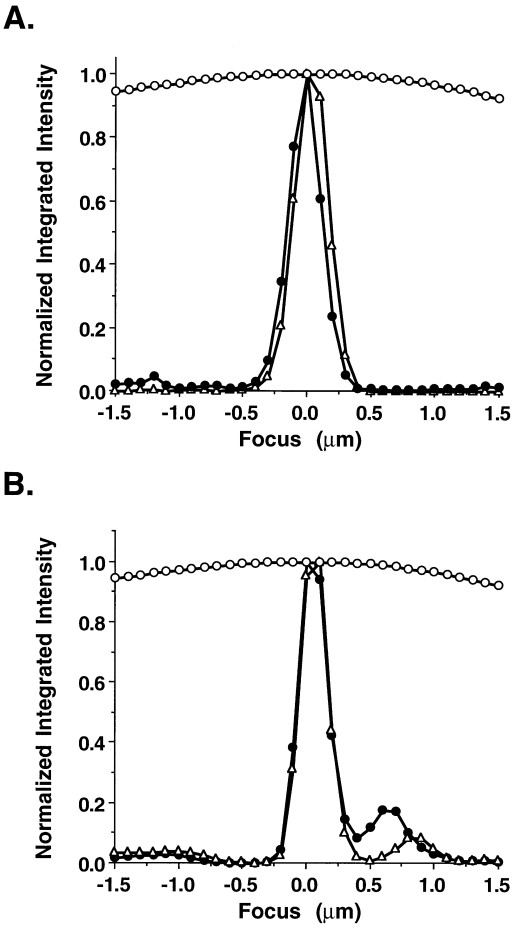

Fig. 4. Deconvolution of bead images with mismatched OTFs. Sensitivity of deconvolution to choice of OTF was assayed by deconvolving PSFs with their associated complex OTFs and OTFs generated from mismatched PSFs. Each panel shows integrated intensity decays obtained from a given PSF before deconvolution, and after deconvolution with its associated complex OTF and a complex OTF generated from a slightly mismatched PSF. Deconvolution of a spherically aberrated PSF with an OTF generated from a PSF manifesting spherical aberration of the same sign usually yields a good deconvolution. In contrast, deconvolution of a spherically aberrated PSF with a real OTF generated from an unaberrated PSF, or with a complex OTF generated from a PSF manifesting a different kind of spherical aberration, often fails to yield a good deconvolution. (A) 60× PSF (n_D^{25} = 1·5230) before deconvolution (○); after deconvolution with its associated complex OTF (●); and after deconvolution with an OTF derived from a PSF recorded with a different oil (n_D^{25} = 1·5300) that gives a positive optical path length error (△). (B) 60× PSF (n_D^{25} = 1·5104) before deconvolution (○); after deconvolution with its associated complex OTF (●); and after deconvolution with an OTF derived from a PSF recorded with a different oil (n_D^{25} = 1·5120) that gives a negative optical path length error (△).

OTFs derived from similar, but not identical, PSFs, the integrated intensity decays and power spectra obtained were remarkably similar to those obtained when the PSFs were deconvolved with their perfectly matched OTFs (Fig. 4). In general, good restoration of the point object was achieved as long as the path length error of the PSF and OTF had the same sign, e.g. an aberrated PSF with a negative optical path length error was deconvolved effectively with any OTF derived from a PSF with, correspondingly, a negative optical path length error. Thus, our iterative, constrained three-dimensional deconvolution approach will tolerate some degree of PSF/OTF mismatch, and exact knowledge of the OTF is not required for accurate reconstruction of an object. This, in turn, implies that a relatively small library of OTFs that spans common types of image aberration will suffice for high-quality deconvolution of most images.

Deconvolution of aberrated biological images

Not surprisingly, we find that images of biological specimens are frequently spherically aberrated. Spherical aberration arises inevitably in multi-wavelength images and frequently in images of samples that are far from the coverslip (Gibson & Lanni, 1991; Hell *et al.*, 1993). In the latter case, it is often difficult to find an oil that will correct for the spherical aberration introduced when light passes through a considerable length of the solution surrounding the sample, and the result is a spherically aberrated image.

An example of a spherically aberrated biological image is shown in Fig. 5. Initially this aberrated image was deconvolved with the real OTF collected with the 60× Olympus objective. The large residual asymmetry and amount of out-of-focus light in the deconvolved image (Fig. 5B,E) indicate that the deconvolution with this OTF was relatively poor. The image was then deconvolved with a series of complex OTFs generated from PSFs from the appropriate spherical aberration class. All of these OTFs generated a reduction in axial asymmetry and in the amount of out-of-focus light (Fig. 5C,F), indicating that deconvolution with the appropriate complex OTF is superior to deconvolution with the real OTF. For the *Drosophila* image shown in Fig. 5, deconvolution with complex OTFs ($n_D^{25} = 1{\cdot}5180$ and $1{\cdot}5230$) produced, respectively, images with 4·3- and 4·8-fold higher contrast than did deconvolution with the real OTF. However, deconvolution with a complex OTF generated from an even more heavily aberrated PSF ($n_D^{25} = 1{\cdot}5300$) produced slightly lower (3·4-fold) relative improvement in contrast. Thus, for typical biological images a reasonably accurate choice of OTF will yield most of the benefit from deconvolution.

Discussion

Effective deblurring of images through deconvolution requires an accurate knowledge of the PSF, which is quite sensitive to optical conditions. Indeed, the PSF depends on the refractive index of the objective immersion oil and on the refractive index of the biological sample, making it sample dependent. Moreover, as shown here, this sensitivity to

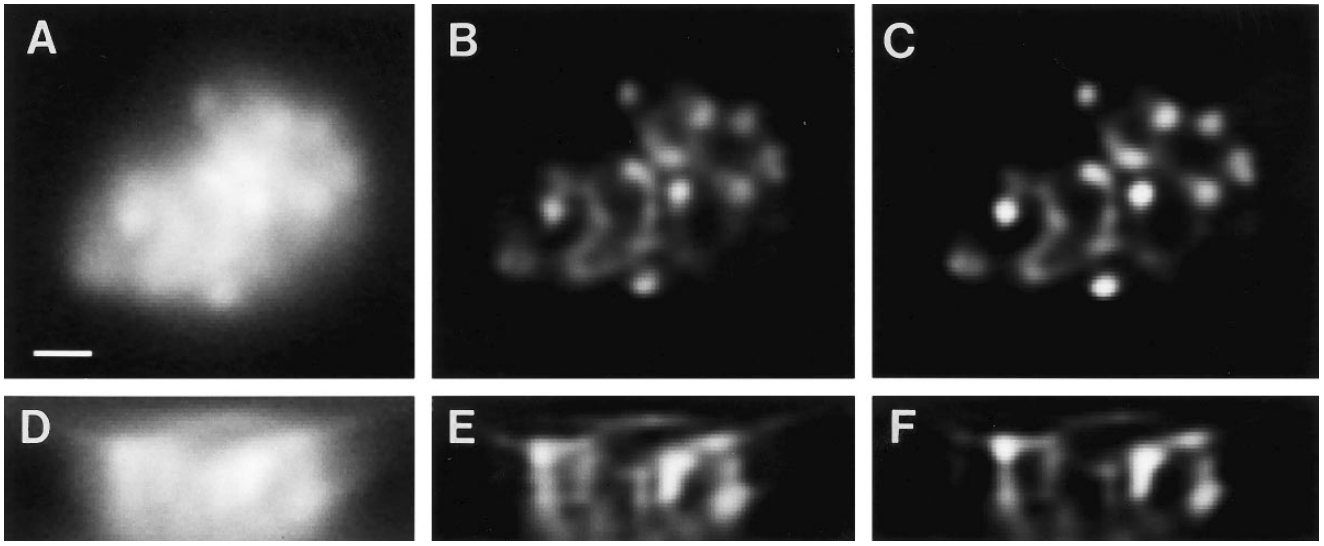

Fig. 5. Spherical aberration and deconvolution of biological images. Images of *Drosophila* embryonic chromosomes during metaphase collected using an Olympus 60×/1·4-NA objective; chromosomes were stained with DAPI. Optical sections were collected at 0·2-μm intervals and then restored using constrained iterative deconvolution. (A,D) Undeconvolved images; (B,E) images deconvolved with an axially symmetric PSF; (C,F) images deconvolved with an axially asymmetric PSF. (A,B,C) Optical section from a three-dimensional data set; (D,E,F) orthogonal views from the data sets in (A,B,C), respectively. Samples were prepared following the protocol given in Hiraoka *et al.* (1990b). Scale bar = 1 μm.

refractive index implies that the PSF is also wavelength dependent, since refractive indices vary with wavelength. The sensitivity of the PSF to optical conditions implies that different OTFs should be used to deconvolve images collected under significantly different optical conditions. Images collected under non-optimal imaging conditions will manifest some degree of spherical aberration; these images should be deconvolved with an OTF generated from a PSF manifesting a similar degree of spherical aberration.

Generating an OTF library

Optimal restoration of a spherically aberrated image requires deconvolution with an OTF possessing approximately the correct aberration characteristics. It is therefore important to have access to a library of PSFs and OTFs that includes a range of optical path length errors. Since PSFs and OTFs are wavelength dependent, an OTF library can be generated using beads (diameter $< 0{\cdot}15\ \mu$m) impregnated with fluorophores with a variety of spectral characteristics; OTFs most appropriate for deconvolving red, green and blue images could then be generated from beads of matching colour.

Significantly, for the lenses we have examined, most of the PSF wavelength-dependent effects are actually a result of spherical aberration (Figs. 1B and 2A). Therefore, the PSF library can be simplified by recording PSFs having different degrees of spherical aberration at a fixed wavelength using oils with different refractive indices. For deconvolution of an image collected at a different wavelength, we simply scale the sampling interval of the OTF containing the appropriate amount of spherical aberration by the ratio of the wavelengths of the image and OTF. This is currently the most straightforward method of generating the OTF library, which typically contains 5–10 OTFs for a given lens.

Ideally, a PSF should be measured or derived from the sample itself (Liu & Holmes, 1993; Loew *et al.,* 1993; Moore *et al.,* 1993). In practice, this is difficult in thick samples like *Drosophila* embryos that contain significant background intensity. The results shown in Fig. 4 suggest that the quality of image restoration is not affected by small differences in optical path length error between the image and the OTF, indicating that the small OTF library can be used for the majority of images collected.

It is also worth noting that an OTF library must be generated for each lens because even high-quality lenses can differ significantly in their aberration characteristics. Careful examination of Fig. 1(A,B) shows that the Olympus lens has more intrinsic spherical aberration at 635 nm than the Nikon lens; under optimal imaging conditions the PSF obtained from the Nikon lens is more radially and axially symmetric and more closely matches the theoretical PSF for these lenses (data not shown). In addition, the OTF of the Nikon 100× extends to higher resolution than the OTF of the Olympus lens, especially along the optical axis. In these respects, the Nikon is a better lens; however, the Olympus lens transmits more light than the Nikon. We have also characterized a Nikon 60×/1·4-NA objective; again, its PSF more closely matches the theoretical PSF than does the PSF of the Olympus 60×/1·4-NA, but its transmittance is lower. Thus, the relative usefulness of these lenses is determined largely by the application.

Aberration and dispersion in biological samples

To this point, we have focused primarily on dispersion in the objective lens immersion oil and its role in generating image aberrations. However, the refractive index of a biological sample also is a function of wavelength, leading to a further source of wavelength-dependent spherical aberration. Moreover, since biological samples have a finite thickness and are not always immediately adjacent to the coverslip, image aberration can arise because point sources of light far from the coverslip are not optimally imaged by the objective lens. Indeed, we have observed both of these effects in our own experiments with *Drosophila* tissues.

The spherical aberration induced in an image by the finite thickness of the sample has been analysed both theoretically and experimentally (Gibson & Lanni, 1991; Hell *et al.,* 1993). It was found that if the sample is less than about 5 μm thick, the images of point sources of light at the bottom and top of the sample are not radically different, and depth-dependent spherical aberration can probably be neglected. However, this conclusion is based on theoretical calculations that assume a fixed refractive index for the biological sample of 1·33 (water), and experimental results obtained for beads embedded in agarose. Since biological systems are very complex and contain significant refractive index heterogeneities, these models may not be completely accurate. Careful examination of *in situ* DNA hybridization signals, which are in effect PSFs, may further help to elucidate the effects that the properties of biological samples have on image aberration. Clearly the most accurate reconstruction will be obtained with an OTF that includes the path length error generated by the tissue itself as well as the focus dependence of spherical aberration. However, two lines of evidence suggest that high-quality deconvolution of images of thick objects can be achieved without introducing this complexity into the deconvolution algorithm. First, we have shown here that some mismatch between the aberration in the PSF used for deconvolution and the actual sample PSF(s) does not significantly compromise the quality of deconvolution achieved. Second, our laboratory has recently obtained images of polytene nuclei embedded in acrylamide that are up to 50 μM below the coverslip (Urata *et al.,* 1995). These images have deconvolved very well despite the considerable distance between the object and coverslip.

Multi-wavelength imaging and confocal microscopy

The observations and ideas discussed here also have direct implications for confocal imaging. In confocal microscopy, the sample is both illuminated and viewed through a pinhole. The resultant total PSF is, at best, the product of the individual excitation and emission PSFs. The effect of spherical aberration is thus two-fold: reduction in image resolution and a significant loss of signal (Hell *et al.,* 1993). In multi-wavelength confocal imaging, the extent of the resolution and signal reduction will be different for each fluorophore because each wavelength component will be spherically aberrated to a different degree. This will complicate any attempt to make quantitative comparisons of intensities obtained from different fluorophores (e.g. ratio imaging), or from fluorophores at different depths in a sample using confocal microscopy. Again, deconvolution approaches can be used to remedy this situation, although the variation of the PSF with depth may have to be taken into account, as discussed above.

Choosing an OTF

There are both quantitative and qualitative methods of choosing the OTF that will best deconvolve an image. Although smallness of the *R* factor (defined in Eq. 3) is frequently used as a measure of deconvolution quality (Ross *et al.,* 1977; Shaw & Rawlins, 1991), we have found that it is not always a reliable measure of the relative quality of deconvolution achieved with different OTFs. Strictly, the *R* factor measures the degree of convergence of the deconvolution process. Since it is generally 'easier' to deconvolve with a narrower PSF, a PSF that is too narrow will invariably give a lower *R* factor, but only a partially deblurred image. In the extreme, deconvolution of an image with an infinitely narrow PSF (delta function) would immediately converge and yield an *R* factor of zero, but would make no changes to the image.

Alternative quantitative measures of deconvolution quality include contrast enhancement, widths of power spectra (Hiraoka *et al.,* 1990a) and axial resolution (Fay *et al.,* 1989; Hiraoka *et al.,* 1990a). We use all of these to help assess deconvolution quality. One approach that we are pursuing is to use axial and radial contrast and the *R* factor to develop a scheme for automatically choosing the optimal member of a library by performing three or five trial deconvolutions at reduced resolution. From this, the best PSF could then be chosen for more extensive deconvolution at full resolution.

Because there is some flexibility involved, in many cases it may be quite sufficient to choose the correct PSF based on visual inspection of the data set itself. Examination of *XZ* views of the undeconvolved image should be sufficient to decide the degree and direction of the spherical aberration present, if any (Figs 1 and 2). Once the aberration pattern in the image has been characterized, the basic type of OTF that should be used for deconvolution is determined by matching the aberration in the image to that in the PSF from which the OTF is derived. This simple method has permitted us markedly to improve deconvolution of spherically aberrated biological images (Fig. 5).

In addition to image degradation produced by spherical aberration, there are numerous other forms of aberration, such as coma, astigmatism, non-planar effects, etc. One or more of these aberrations are probably responsible for the prominent radial asymmetry observed in most empirical PSFs. This issue is the focus of current study.

Acknowledgments

We thank Dr James Abney for a critical reading of the manuscript. We also thank Olympus, Inc. and Nikon, Inc. for making multiple copies of their high-NA lenses available to us for characterization and comparison. This work was supported by grants from the National Institutes of Health to J.W.S. (GM-25101) and D.A.A. (GM-31627). Much of this work was supported by the Howard Hughes Medical Institute. D.A.A. is a Howard Hughes Investigator.

References

Agard, D.A. (1984) Optical sectioning microscopy: cellular architecture in three dimensions. *Ann. Rev. Biophys. Bioeng.* **13,** 191–219.

Agard, D.A., Hiraoka, Y., Shaw, P. & Sedat, J.W. (1989) Fluorescence microscopy in three dimensions. *Methods Cell Biol.* **30,** 353–377.

Born, M. & Wolf, E. (1980) *Principles of Optics.* Pergamon Press, New York, NY.

Cargille Laboratories Catalog. (1994) Cargille Laboratories, Cedar Grove, NJ.

Carrington, W. (1990) Image restoration in 3D microscopy with limited data. *Proc. Soc. Photo-Opt. Instrum. Eng.* **1205,** 72–83.

Castleman, K.R. (1979) *Digital Image Processing.* Prentice Hall, Englewood Cliffs, NJ.

Chen, H., Swedlow, J.R., Grote, M., Sedat, J.W. & Agard, D.A. (1995) The collection, processing, and display of digital three-dimensional images of biological specimens. *Handbook of Biological Confocal Microscopy,* 2nd edn (ed. by J. Pawley), pp. 197–210. Plenum Press, New York.

Conchello, J. & Hansen, E. (1990) Enhanced 3D reconstruction from confocal scanning microscope images. 1: Deterministic and maximum likelihood reconstructions. *Appl. Opt.* **29,** 3795–3804.

Denk, W., Strickler, J.H. & Webb, W.W. (1990) Two-photon laser scanning fluorescence microscopy. *Science,* **248,** 73–76.

Fay, F.S., Carrington, W. & Fogarty, K.E. (1989) 3-D molecular distribution — digital imaging. *J. Microsc.* **153,** 133–149.

Frieden, B.R. (1969) Maximum attainable MTF for rotationally symmetric lens systems. *J. Opt. Soc. Am.* **59,** 402–406.

Gibson, S.F. & Lanni, F. (1991) Experimental test of an analytical model of aberration in an oil-immersion objective lens used in three-dimensional light microscopy. *J. Opt. Soc. Am. A,* **8,** 1601–1613.

Hell, S., Reiner, G., Cremer, C. & Stelzer, E.H.K. (1993) Aberrations

in confocal fluorescence microscopy induced by mismatches in refractive index. *J. Microsc.* **169,** 391–405.

Hiraoka, Y., Agard, D.A. & Sedat, J.W. (1990a) Temporal and spatial coordination of chromosome movement, spindle formation, and nuclear envelope breakdown during prometaphase in *Drosophila melanogaster* embryos. *J. Cell Biol.* **111,** 2815–2828.

Hiraoka, Y., Sedat, J.W. & Agard, D.A. (1990b) Determination of the three-dimensional imaging properties of a light microscope system: partial confocal behavior in epifluorescence microscopy. *Biophys. J.* **57,** 325–333.

Hiraoka, Y., Swedlow, J.R., Paddy, M.R., Agard, D.A. & Sedat, J.W. (1991) Three-dimensional multiple-wavelength fluorescence microscopy for the structural analysis of biological phenomena. *Seminars Cell Biol.* **2,** 153–165.

Inoue, S. (1986) *Video Microscopy.* Plenum, New York, NY.

Koshy, M., Agard, D.A. & Sedat, J.W. (1990) Solution of toeplitz systems for the restoration of 3-D optical sectioning microscopy data. *Bioimag. Two-Dimens. Spectrosc. SPIE,* **1205,** 64–70.

Liu, Y.-H. & Holmes, T.J. (1993) 2D and 3D fluorescence microscopy by maximum likelihood estimation: micrograph results. *MSA Bull.* **23,** 189–198.

Loew, L.M., Tuft, R.A., Carrington, W. & Fay, F.S. (1993) Imaging in five dimensions: time-dependent membrane potentials in individual mitochondria. *Biophys. J.* **65,** 2396–2407.

Moore, E.D., Etter, E.F., Philipson, K.D., Carrington, W.A., Fogarty, K.E., Lifshitz, L.F. & Fay, F.S. (1993) Coupling of the Na^+/Ca^{2+} exchanger, Na^+/K^+ pump and sarcoplasmic reticulum in smooth muscle. *Nature,* **365,** 657–660.

Pawley, J. (1995) *Handbook of Biological Confocal Microscopy,* 2nd edn. Plenum Press, New York.

Ross, M.J., Klymkowsky, M.W., Agard, D.A. & Stroud, R.M. (1977) Structural studies of a membrane-bound acetylcholine receptor from *Torpedo californica. J. Mol. Biol.* **116,** 635–659.

Shaw, P.J. (1990) Three-dimensional optical microscopy using tilted views. *J. Microsc.* **158,** 165–172.

Shaw, P.J. & Rawlins, D.J. (1991) The point-spread of a confocal microscope: its measurement and use in deconvolution of 3-D data. *J. Microsc.* **163,** 151–165.

Taylor, D.L., Nederlof, M., Lanni, F. & Waggoner, A.S. (1992) The new vision of light microscopy. *Am. Sci.* **80,** 322–335.

Urata, Y., Parmelee, S.J., Agard, D.A. & Sedat, J.W. (1995) A three-dimensional structural dissection of Drosophila polytene chromosomes. *J. Cell Biol.* **131,** 274–295.

Willis, B., Roysam, B., Turner, J.N. & Holmes, T.J. (1993) Iterative, constrained 3-D image reconstruction of transmitted light bright-field micrographs based on maximum likelihood estimation. *J. Microsc.* **169,** 347–361.